Drivers of abrupt Holocene shifts in West Antarctic ice stream direction determined from combined ice sheet modelling and geologic signatures

Journal Article

Author(s):
Fogwill, C.J.; Turney, Chris; Golledge, N.R.; Rood, D.H.; Hippe, K.; Wacker, L.; Wieler, R.; Rainsley, E.B.; Jones, R.S.

Drivers of abrupt Holocene shifts in West Antarctic ice stream direction determined from combined ice sheet modelling and geologic signatures

C.J. FOGWILL[1], C.S.M. TURNEY[1], N.R. GOLLEDGE[2,3], D.H. ROOD[4], K. HIPPE[5,6], L. WACKER[6], R. WIELER[5], E.B. RAINSLEY[7] and R.S. JONES[2]

[1]*Climate Change Research Centre, University of New South Wales, Sydney, NSW 2052, Australia*
[2]*Antarctic Research Centre, Victoria University of Wellington, Wellington 6140, New Zealand*
[3]*GNS Science, Avalon, Lower Hutt 5011, New Zealand*
[4]*Scottish Universities Environmental Research Centre (SUERC), East Kilbride G75 0QF, UK*
[5]*Institute of Geochemistry and Petrology, ETH Zürich, CH-8092 Zürich, Switzerland*
[6]*Institute for Particle Physics, ETH Zürich, CH-8093 Zürich, Switzerland*
[7]*Unaffiliated*
c.fogwill@unsw.edu.au

Abstract: Determining the millennial-scale behaviour of marine-based sectors of the West Antarctic Ice Sheet (WAIS) is critical to improve predictions of the future contribution of Antarctica to sea level rise. Here high-resolution ice sheet modelling was combined with new terrestrial geological constraints (*in situ* [14]C and [10]Be analysis) to reconstruct the evolution of two major ice streams entering the Weddell Sea over 20 000 years. The results demonstrate how marked differences in ice flux at the marine margin of the expanded Antarctic ice sheet led to a major reorganization of ice streams in the Weddell Sea during the last deglaciation, resulting in the eastward migration of the Institute Ice Stream, triggering a significant regional change in ice sheet mass balance during the early to mid Holocene. The findings highlight how spatial variability in ice flow can cause marked changes in the pattern, flux and flow direction of ice streams on millennial timescales in this marine ice sheet setting. Given that this sector of the WAIS is assumed to be sensitive to ocean-forced instability and may be influenced by predicted twenty-first century ocean warming, our ability to model and predict abrupt and extensive ice stream diversions is key to a realistic assessment of future ice sheet sensitivity.

Introduction

Recent observations of rapidly accelerating West Antarctic outlet glaciers have prompted a radical shift in the way the sensitivity of marine-terminating ice sheets to ocean forcing is viewed (Rignot *et al.* 2014). Critical to this debate is the influence of subglacial topography on marine-based ice sheet dynamics (commonly referred to as the marine ice sheet instability hypothesis) where positive ice-loss feedbacks may occur when the grounding line is both below sea level and within a basin which deepens towards the centre of the ice sheet (Weertman 1974, Thomas & Bentley 1978). Decadal-scale changes consistent with this mechanism have been implicated in several key outlets of the West Antarctic Ice Sheet (WAIS) (Rignot *et al.* 2014), suggesting that even small changes at the margins of the Antarctic ice sheets may trigger far-reaching changes in the interior of the Antarctic ice sheet through ice streams, narrow corridors of enhanced ice flow, which control the mass balance of the

Antarctic ice sheets (Cuffey 2011, Golledge *et al.* 2012, Rignot *et al.* 2014). However, it remains unclear whether such a long-term transformation in ice sheet dynamics will take place, potentially leading to future collapse and associated rapid sea level rise (Bamber *et al.* 2009, Rignot *et al.* 2014). Therefore, understanding the mechanisms that control enhanced flow is key to predicting future WAIS stability (Cuffey 2011, Rignot *et al.* 2011).

The Weddell Sea embayment (WSE) of Antarctica potentially offers significant insights into this debate. Today the extensive Filchner-Ronne Ice Shelf of the Weddell Sea is partially sustained by the inflow of nine large ice streams that together drain 22% of Antarctica, yet its detailed history of deglaciation since the Last Glacial Maximum (LGM), and particularly during the Holocene, remains poorly constrained (Larter *et al.* 2012, Stolldorf *et al.* 2012, Siegert *et al.* 2013, Hillenbrand *et al.* 2014). Whilst contemporary satellite remote sensing suggests a modest elevation of the ice sheet surface across much of the region in recent decades (Rignot *et al.* 2011), there is

a mounting body of evidence that indicates ice stream drainage patterns in the region were markedly different during the Holocene, implying that the region is sensitive to external forcings and thus may be vulnerable to past and potentially future change (Siegert *et al.* 2013). Evidence for this comes from interpretations of airborne radar-echo sounding (RES), marine geophysical investigations and satellite imagery, which suggests there has been substantial late Holocene reconfiguration of the ice streams in the Weddell Sea; however, the timing and, critically, the mechanisms driving these changes remain uncertain (Siegert *et al.* 2013). Understanding these mechanisms is critical given twenty-first century projections of ocean warming in the region (Hellmer *et al.* 2012, Fogwill *et al.* 2014), and the presence of extensive subglacial basins upstream of the present-day grounding line (Ross *et al.* 2012).

To assess the response of ice stream configuration in the Weddell Sea to external forcing since the LGM this study generates new high-resolution, whole-continent ice sheet model simulations for comparison with detailed terrestrial and marine geochronological constraints. The combination of these detailed geological ice sheet constraints with the high-resolution palaeo ice sheet model simulations to examine the drivers of ice sheet change over the last 20 000 years allows the response of ice streams to ocean forcing and sea level rise during the transition between the glacial and interglacial world to be investigated, improving our understanding of ice dynamic responses of the ice streams in the Weddell Sea and wider WAIS to ocean perturbations. Recent studies (e.g. Larter *et al.* 2012) postulate that three major cross-shelf troughs may have played a role in controlling WSE dynamics during deglaciation, the Rutford Trough (or Ronne Depression), the Hughes Trough and the Thiel Trough (or Filchner or Crary Trough). The combination of high-resolution ice sheet modelling and geological constraints in this study allows the role of these features to be explored more fully.

Ice sheet model simulations

Here the results of high-resolution ice sheet modelling experiments that investigate the dynamic response of an LGM-configuration Antarctic ice sheet to ocean forcing (Golledge *et al.* 2012, 2013) are presented. The parallel ice sheet model (PISM) is used, a 3-D, thermomechanical, continental ice sheet model, constrained by published geological data that define lateral and vertical extents of the expanded Antarctic ice sheets around the time of the LGM (Golledge *et al.* 2012). The model combines the shallow-ice and shallow-shelf approximation equations across the entire domain. Therefore, the model is able to capture the dynamic behaviour within grounded ice
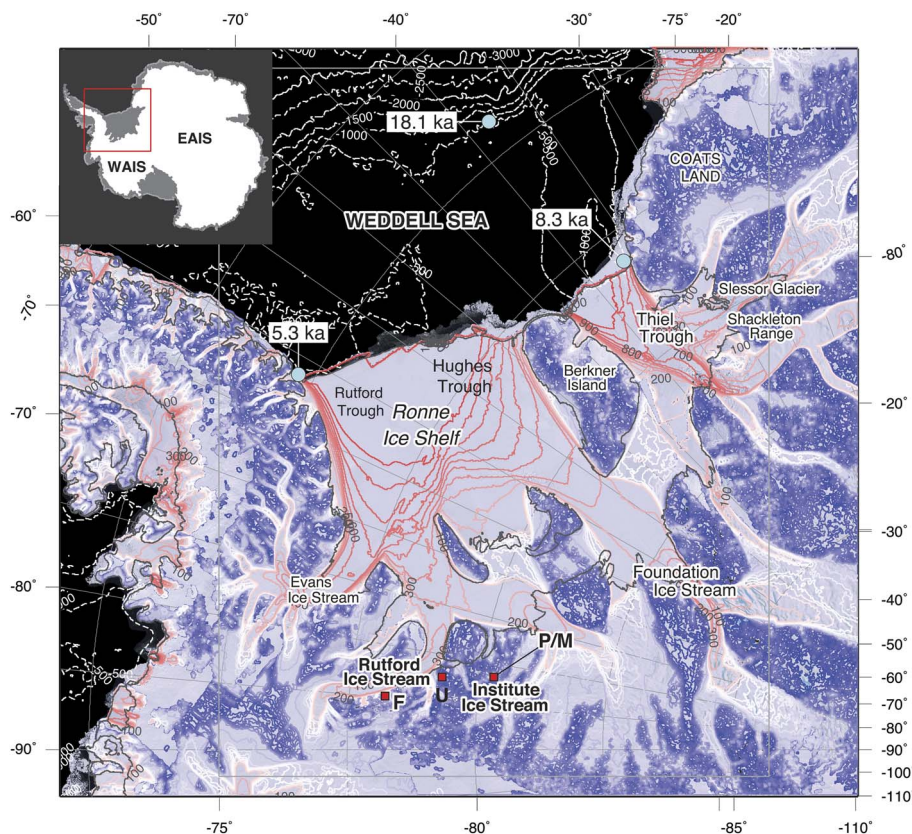
Fig. 1. Weddell Sea embayment (WSE) indicating the sampling locations next to the Rutford and Institute ice streams. Ice sheet surface velocity data (Rignot *et al.* 2011) highlight the locations of the major ice streams in light colours, and ice rises and slow moving regions in the WSE in darker blue. The sites of marine cores and associated minimum ages for grounding line retreat based upon marine radiocarbon ages (Hillenbrand *et al.* 2014) are also shown. F = Flower Hills, U = Union Glacier, P/M = Patriot and Marble hills.

of Antarctic ice sheets and simulate the drawdown of interior ice by ice streams at high resolution (5 km). In this study, the model uses proxy-based interpretations of oceanic (Lisiecki *et al.* 2005, Imbrie *et al.* 2006) and atmospheric (Petit *et al.* 1999) changes during the last glacial cycle and employs boundary distributions from modified Bedmap topography (Le Brocq *et al.* 2010), temperature and precipitation fields from gridded datasets (Comiso 2000, Van de Berg 2006), and a spatially varying geothermal heat flux interpolation (Shapiro & Ritzwoller 2004).

The ice sheet model computes ice thickness and temperature changes, isostatic depression of topography, migration of grounding lines and the growth of ice shelves. Interaction between modelled ice shelves and their surrounding ocean is accounted for using a mass balance determination based on heat flux across the ice-water boundary. Our perturbation experiments use isochronous changes to oceanic heat flux and sea level values. The ice sheet model simulations are based on ocean-perturbation experiments in which the oceanic heat flux and sea level are isochronously increased from 30% to 100% of glacial to interglacial transition values, and by 25 m and 50 m, with respect to LGM values, representative of Holocene values. The response of the ice sheet is considered in terms of changes in velocity and ice thickness which together yield mass flux and, importantly, changes in ice flow direction.

Geological and geochronological constraints

To provide a temporal context for the modelled ice stream response, new and recalibrated existing geochronological data are used to reconstruct the geometric and temporal changes in the ice streams feeding the western part of the Weddell Sea following the LGM. The terrestrial record constrains altitudinal changes of the former ice stream surface, whereas offshore marine records, from radiocarbon dating of glaciomarine sediments overlying the subglacial deposits, constrain the lateral extent of the ice sheet in the WSE. Both are required to reconstruct the 3-D changes in ice stream geometry and investigate palaeo ice volume changes.

Marine geochronological constraints

The limited available analyses of marine sediment cores (including radiocarbon) from the outer and inner continental shelf of the WSE are used to constrain the lateral extent of the ice sheet, and provide the timing of ice sheet grounding line retreat and establishment of open water conditions (Larter *et al.* 2012, Stolldorf *et al.* 2012,
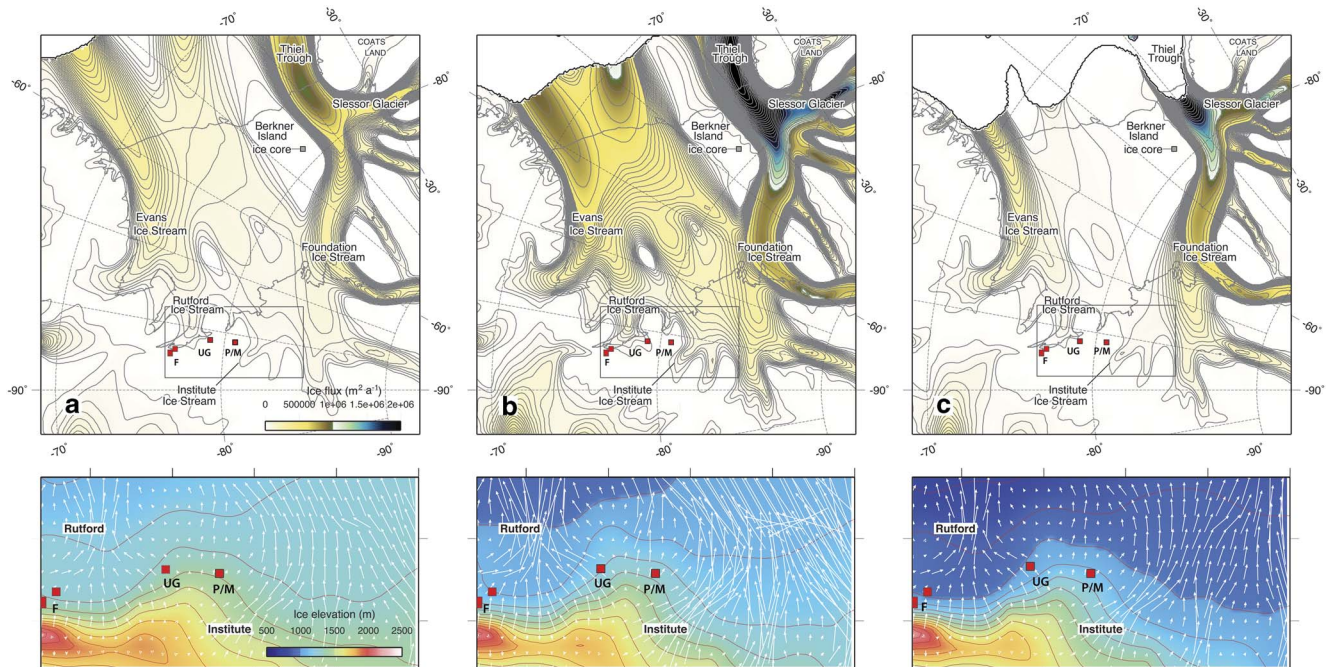
Fig. 2. Simulated regional ice flux (upper panels), together with ice flow direction (white arrows) and ice sheet surface elevation of the Rutford and Institute ice streams (lower panel). **a.** Post-LGM conditions. **b.** Initial response to imposed ocean forcing leads to widespread acceleration of ice flow at principal outlets at *c.* 15 000 model years. **c.** Continued ice recession then leading to capture of the Institute Ice Stream by the Thiel Trough outlet during the late to mid Holocene. Ice flow vectors in the area of interest illustrate the change in flow direction taking place between time slices and red squares show the sample locations. F = Flower Hills, UG = Union Glacier, P/M = Patriot and Marble hills.

Table I. ¹⁰Be cosmogenic isotope data from the Patriot and Marble hills recording changes in the Institute Ice Stream, and data from the Flower Hills and Union Glacier recording changes in the Rutford Ice Stream (Fogwill *et al.* 2012).

Sample name	Latitude (°S)	Longitude (°W)	Elevation (m)	Elevation/ pressure	Thickness (cm)	Density	Shielding[a]	Erosion rate	^{10}Be (at g^{-1})	± ^{10}Be (at g^{-1})[b]	^{10}Be standard	^{26}Al (at g^{-1})	± ^{26}Al (at g^{-1})	^{26}Al standard	^{10}Be exposure age (years) P_{Global}[c]	± External uncertainty (years)	^{10}Be exposure age (years) P_{NZ}[c]	± External uncertainty (years)	Extraction / AMS analysis undertaken at[d]
Patriot Hills																			
CF-01-08	-80	-81	760	ant	5	2.65	0.98	0	1.62E+05	8.24E+03	NIST_27900	0.00E+00	0.00E+00	KNSTD	14 273	1442	16 642	924	ED-SUERC
CF-02-08	-80	-81	760	ant	5	2.65	0.99	0	9.11E+03	1.29E+03	NIST_27900	0.00E+00	0.00E+00	KNSTD	792	132	923	132	ED-SUERC
CF-03-08	-80	-81	762	ant	5	2.65	0.98	0	5.99E+03	4.00E+02	NIST_27900	0.00E+00	0.00E+00	KNSTD	525	58	612	43	ED-SUERC
CF-08-08	-80	-81	936	ant	5	2.65	0.98	0	5.47E+06	5.29E+04	NIST_27900	0.00E+00	0.00E+00	KNSTD	460 394	45 242	548 064	15 009	ED-SUERC
CF-09-08	-80	-81	1004	ant	5	2.65	0.99	0	5.65E+06	6.96E+04	NIST_27900	0.00E+00	0.00E+00	KNSTD	442 082	43 401	525 873	15 036	ED-SUERC
CF-13-08	-80	-81	989	ant	5	2.65	0.97	0	1.06E+06	1.75E+04	NIST_27900	0.00E+00	0.00E+00	KNSTD	78 420	7071	91 722	2563	ED-SUERC
CF-14-08	-80	-81	935	ant	5	2.65	0.97	0	4.61E+05	1.25E+04	NIST_27900	0.00E+00	0.00E+00	KNSTD	35 352	3245	41 269	1449	ED-SUERC
CF-17-08	-80	-81	826	ant	5	2.65	0.97	0	5.77E+05	1.54E+04	NIST_27900	0.00E+00	0.00E+00	KNSTD	48 841	4493	57 036	1992	ED-SUERC
CF-19-08	-80	-81	816	ant	5	2.65	0.97	0	2.66E+05	6.10E+03	NIST_27900	0.00E+00	0.00E+00	KNSTD	22 568	2039	26 325	838	ED-SUERC
CF-21-08	-80	-81	774	ant	5	2.65	0.99	0	4.86E+04	1.25E+03	NIST_27900	0.00E+00	0.00E+00	KNSTD	4176	379	4868	164	ED-SUERC
CF-24-08	-80	-81	761	ant	5	2.65	0.97	0	3.64E+04	4.84E+02	NIST_27900	0.00E+00	0.00E+00	KNSTD	3227	284	3761	96	ED-SUERC
CF-25-08	-80	-81	940	ant	5	2.65	0.97	0	6.25E+05	1.59E+04	NIST_27900	0.00E+00	0.00E+00	KNSTD	47 870	4385	55 912	1898	ED-SUERC
CF-28-08	-80	-81	879	ant	5	2.65	0.97	0	6.89E+05	1.80E+04	NIST_27900	0.00E+00	0.00E+00	KNSTD	55 760	5129	65 143	2251	ED-SUERC
CF-29-08	-80	-81	879	ant	5	2.65	0.97	0	3.95E+05	1.05E+04	NIST_27900	0.00E+00	0.00E+00	KNSTD	31 777	2910	37 086	1286	ED-SUERC
CF-31-08	-80	-81	863	ant	5	2.65	0.97	0	1.79E+05	4.11E+03	NIST_27900	0.00E+00	0.00E+00	KNSTD	14 541	1311	16 958	539	ED-SUERC
PAT-01-MJB	-80	-81	1092	ant	5	2.65	0.99	0	1.34E+05	3.79E+03	NIST_27900	0.00E+00	0.00E+00	KNSTD	8748	801	10 204	365	ED-SUERC
PAT-03-MJB	-80	-81	1009	ant	5	2.65	0.97	0	8.70E+04	2.65E+04	NIST_27900	0.00E+00	0.00E+00	KNSTD	6214	1971	7246	2217	ED-SUERC
PAT-04-CJF	-80	-81	933	ant	5	2.65	0.97	0	4.11E+05	1.11E+04	NIST_27900	0.00E+00	0.00E+00	KNSTD	31 542	2892	36 816	1289	ED-SUERC
PAT-04-MJB	-80	-81	998	ant	5	2.65	0.99	0	1.39E+05	1.00E+04	NIST_27900	0.00E+00	0.00E+00	KNSTD	9833	1112	11 468	864	ED-SUERC
PAT-05-MJB	-80	-81	954	ant	5	2.65	0.97	0	9.37E+04	1.08E+04	NIST_27900	0.00E+00	0.00E+00	KNSTD	7018	1015	8184	962	ED-SUERC
PAT-08-CJF	-80	-81	1004	ant	5	2.65	0.97	0	5.36E+06	8.50E+04	NIST_27900	0.00E+00	0.00E+00	KNSTD	426 237	41 944	506 588	15 519	ED-SUERC
PAT-10-CJF	-80	-81	1002	ant	5	2.65	0.97	0	5.90E+06	1.05E+05	NIST_27900	0.00E+00	0.00E+00	KNSTD	475 596	47 601	566 645	18 410	ED-SUERC
PAT-13-CJF	-80	-81	978	ant	5	2.65	0.97	0	5.09E+06	9.31E+04	NIST_27900	0.00E+00	0.00E+00	KNSTD	412 538	40 667	489 952	15 778	ED-SUERC
PAT-14-CJF	-80	-81	968	ant	5	2.65	0.97	0	1.09E+06	2.07E+04	NIST_27900	0.00E+00	0.00E+00	KNSTD	82 187	7459	96 140	2844	ED-SUERC
PAT-15-CJF	-80	-81	965	ant	5	2.65	0.97	0	1.05E+06	1.42E+04	NIST_27900	0.00E+00	0.00E+00	KNSTD	79 319	7113	92 773	2432	ED-SUERC
PAT-16-CJF	-80	-81	960	ant	5	2.65	0.97	0	7.17E+05	1.99E+04	NIST_27900	0.00E+00	0.00E+00	KNSTD	54 058	4996	63 158	2263	ED-SUERC
PAT-18-CJF	-80	-81	774	ant	5	2.65	0.97	0	5.36E+06	8.50E+04	NIST_27900	0.00E+00	0.00E+00	KNSTD	534 920	54 146	638 944	20 264	ED-SUERC
PAT-20-CJF	-80	-81	772	ant	5	2.65	0.97	0	9.52E+05	1.03E+04	NIST_27900	0.00E+00	0.00E+00	KNSTD	85 311	7629	99 769	2485	ED-SUERC
PAT-21-CJF	-80	-81	769	ant	5	2.65	0.97	0	3.97E+05	6.77E+03	NIST_27900	0.00E+00	0.00E+00	KNSTD	35 230	3146	41 113	1148	ED-SUERC
PAT-24-CJF	-80	-81	777	ant	5	2.65	0.97	0	3.77E+05	7.76E+03	NIST_27900	0.00E+00	0.00E+00	KNSTD	33 201	2988	38 742	1172	ED-SUERC
PAT-25-CJF	-80	-81	775	ant	5	2.65	0.97	0	4.42E+05	6.97E+03	NIST_27900	0.00E+00	0.00E+00	KNSTD	39 051	3481	45 580	1239	ED-SUERC
PAT-26-CJF	-80	-81	775	ant	5	2.65	0.99	0	5.43E+05	1.16E+04	NIST_27900	0.00E+00	0.00E+00	KNSTD	47 121	4265	55 023	1701	ED-SUERC
Marble Hills																			
CF-222-08	-80	-82	1126	ant	5	2.65	0.98	0	6.21E+05	7.61E+03	NIST_27900	0.00E+00	0.00E+00	KNSTD	40 106	3554	46 844	1183	ED-SUERC
CF-223-08	-80	-82	1126	ant	5	2.65	0.99	0	7.06E+05	1.86E+04	NIST_27900	0.00E+00	0.00E+00	KNSTD	45 200	4149	52 808	1828	ED-SUERC
CF-224-08	-80	-82	1126	ant	5	2.65	0.99	0	9.57E+05	2.67E+04	NIST_27900	0.00E+00	0.00E+00	KNSTD	61 519	5700	71 923	2591	ED-SUERC
CF-225-08	-80	-82	1032	ant	5	2.65	0.99	0	8.51E+05	2.33E+04	NIST_27900	0.00E+00	0.00E+00	KNSTD	59 198	5472	69 192	2462	ED-SUERC
CF-227-08	-80	-82	1032	ant	5	2.65	0.99	0	5.35E+05	1.48E+04	NIST_27900	0.00E+00	0.00E+00	KNSTD	37 011	3405	43 219	1538	ED-SUERC
CF-228-08	-80	-82	986	ant	5	2.65	0.99	0	8.09E+04	1.74E+03	NIST_27900	0.00E+00	0.00E+00	KNSTD	5776	518	6736	206	ED-SUERC
CF-229-08	-80	-82	986	ant	5	2.65	0.99	0	6.95E+04	1.66E+03	NIST_27900	0.00E+00	0.00E+00	KNSTD	4961	447	5785	187	ED-SUERC
CF-230-08	-80	-82	950	ant	5	2.65	0.99	0	1.28E+05	3.06E+03	NIST_27900	0.00E+00	0.00E+00	KNSTD	9436	852	11 005	357	ED-SUERC
CF-231-08	-80	-82		ant	5	2.65	0.99	0	4.52E+03	2.97E+02	NIST_27900	0.00E+00	0.00E+00	KNSTD			388	27	ED-SUERC
MAR-02-CJF	-80	-82	1385	ant	5	2.65	0.99	0	7.27E+06	1.76E+05	NIST_27900	0.00E+00	0.00E+00	KNSTD	411 772	41 226	489 394	18 045	ED-SUERC
MAR-04-mjb	-80	-82	1246	ant	5	2.65	0.99	0	3.61E+06	8.94E+04	NIST_27900	2.13E+07	3.99E+05	KNSTD	218 357	20 839	257 099	9043	ED-SUERC
MAR-05-MJB	-80	-82	1192	ant	5	2.65	0.97	0	1.19E+05	2.99E+03	NIST_27900	0.00E+00	0.00E+00	KNSTD	7287	660	8501	283	ED-SUERC
MAR-06-MJB	-80	-82	1166	ant	5	2.65	0.97	0	1.27E+05	5.72E+03	NIST_27900	5.98E+06	1.36E+06	KNSTD	7949	779	9272	465	ED-SUERC
MAR-07-cjf	-80	-82	1300	ant	5	2.65	0.99	0	5.37E+05	1.22E+04	NIST_27900	3.17E+06	1.46E+06	KNSTD	29 662	2683	34 640	1099	ED-SUERC
MAR-08-CJF	-80	-82	1302	ant	5	2.65	0.99	0	6.45E+05	5.59E+04	NIST_27900	0.00E+00	0.00E+00	KNSTD	35 622	4410	41 612	3757	ED-SUERC
MAR-08-MJB	-80	-82	1002	ant	5	2.65	0.97	0	9.55E+04	9.43E+02	NIST_27900	0.00E+00	0.00E+00	KNSTD	6863	601	8004	192	ED-SUERC
MAR-09-cjf	-80	-82	1305	ant	5	2.65	0.99	0	2.95E+05	2.20E+03	NIST_27900	0.00E+00	0.00E+00	KNSTD	16 174	1416	18 878	436	ED-SUERC
MAR-10-CJF	-80	-82	1280	ant	5	2.65	0.99	0	4.65E+06	1.04E+05	NIST_27900	0.00E+00	0.00E+00	KNSTD	277 530	26 701	327 679	11 108	ED-SUERC
MAR-10-MJB	-80	-82	974	ant	5	2.65	0.99	0	1.70E+05	3.18E+03	NIST_27900	0.00E+00	0.00E+00	KNSTD	12 284	1095	14 328	413	ED-SUERC
MAR-11_cjf	-80	-82	1280	ant	5	2.65	0.99	0	2.96E+05	9.64E+03	NIST_27900	0.00E+00	0.00E+00	KNSTD	16 564	1543	19 334	761	ED-SUERC
MAR-11-MJB	-80	-82	810	ant	5	2.65	0.99	0	2.73E+04	6.39E+02	NIST_27900	0.00E+00	0.00E+00	KNSTD	2271	204	2647	85	ED-SUERC

Table I: Continued

Sample name	Latitude (°S)	Longitude (°W)	Elevation (m)	Elevation/ pressure	Thickness (cm)	Density	Shielding[a]	Erosion rate	^{10}Be (at g^{-1})	± ^{10}Be (at g^{-1})[b]	^{10}Be standard	^{26}Al (at g^{-1})	± ^{26}Al (at g^{-1})	^{26}Al standard	^{10}Be exposure age (years) P_{Global}[c]	± External uncertainty (years)	^{10}Be exposure age (years) P_{NZ}[c]	± External uncertainty (years)	Extraction /AMS analysis undertaken at[d]
MAR-12-MJB	-80	-82	807	ant	5	2.65	0.97	0	3.48E+04	2.11E+03	NIST_27900	0.00E+00	0.00E+00	KNSTD	2962	314	3452	223	ED-SUERC
MAR-13-CJF	-80	-82	1112	ant	5	2.65	0.99	0	3.38E+06	7.60E+04	NIST_27900	0.00E+00	0.00E+00	KNSTD	229 135	21 782	269 865	9039	ED-SUERC
MAR-16-cjf	-80	-82	1117	ant	5	2.65	0.99	0	7.66E+05	1.83E+04	NIST_27900	4.79E+06	1.01E+05	KNSTD	49 466	4512	57 801	1895	ED-SUERC
MAR-17-MJB	-80	-82	959	ant	5	2.65	0.99	0	1.17E+06	2.62E+04	NIST_27900	0.00E+00	0.00E+00	KNSTD	87 256	8000	102 097	3270	ED-SUERC
MAR-18-MJB	-80	-82	943	ant	5	2.65	0.99	0	4.02E+05	8.47E+03	NIST_27900	0.00E+00	0.00E+00	KNSTD	29 968	2699	34 979	1069	ED-SUERC
MAR-19-CJF	-80	-82	1109	ant	5	2.65	0.99	0	5.41E+05	1.01E+04	NIST_27900	0.00E+00	0.00E+00	KNSTD	35 046	3141	40 926	1185	ED-SUERC
MAR-19-MJB	-80	-82	936	ant	5	2.65	0.99	0	4.07E+05	1.26E+04	NIST_27900	0.00E+00	0.00E+00	KNSTD	30 530	2837	35 635	1360	ED-SUERC
MAR-20-MJB	-80	-82	900	ant	5	2.65	0.99	0	3.92E+05	7.40E+03	NIST_27900	0.00E+00	0.00E+00	KNSTD	30 339	2717	35 409	1029	ED-SUERC
MAR-21-cjf	-80	-82	1040	ant	5	2.65	0.99	0	3.44E+06	8.22E+04	NIST_27900	1.49E+07	3.09E+05	KNSTD	249 066	23 894	293 570	10 218	ED-SUERC
MAR-24-cjf	-80	-82	953	ant	5	2.65	0.99	0	4.96E+05	1.20E+04	NIST_27900	2.90E+06	8.03E+04	KNSTD	36 719	3341	42 871	1410	ED-SUERC
MAR-24-MJB	-80	-82	1133	ant	5	2.65	0.99	0	8.12E+05	1.53E+04	NIST_27900	0.00E+00	0.00E+00	KNSTD	51 767	4661	60 498	1768	ED-SUERC
MAR-26-CJF	-80	-82	879	ant	5	2.65	0.99	0	8.18E+04	4.73E+03	NIST_27900	0.00E+00	0.00E+00	KNSTD	6410	670	7473	463	ED-SUERC
Flower Hills																			
FLO-18-CJF	-78	-85	1327	ant	5	2.65	0.985	0	3.73E+05	6.78E+03	NIST_27900	0.00E+00	0.00E+00	KNSTD	20 193	1801	23 573	672	ED-SUERC
FLO-10-CJF	-78	-85	1281	ant	5	2.65	0.985	0	1.00E+07	2.61E+05	NIST_27900	0.00E+00	0.00E+00	KNSTD	659 768	70 868	794 193	33 072	ED-SUERC
FLO-15-CJF	-78	-85	1309	ant	5	2.65	0.985	0	5.62E+06	7.71E+04	NIST_27900	0.00E+00	0.00E+00	KNSTD	333 883	31 952	395 275	11 240	ED-SUERC
FLO-03-CJF	-78	-84	1352	ant	5	2.65	0.985	0	1.05E+06	1.98E+04	NIST_27900	0.00E+00	0.00E+00	KNSTD	56 332	5078	65 865	1926	ED-SUERC
FLO-04-CJF	-78	-84	1335	ant	5	2.65	0.985	0	2.72E+06	5.71E+04	NIST_27900	0.00E+00	0.00E+00	KNSTD	151 396	14 054	177 744	5619	ED-SUERC
FLO-19-CJF	-78	-84	1336	ant	5	2.65	0.985	0	7.62E+05	1.49E+04	NIST_27900	0.00E+00	0.00E+00	KNSTD	41 217	3708	48 160	1426	ED-SUERC
FLO-20-CJF	-78	-84	1335	ant	5	2.65	0.96	0	8.94E+05	1.75E+04	NIST_27900	0.00E+00	0.00E+00	KNSTD	49 706	4483	58 096	1733	ED-SUERC
FLO-17-CJF	-78	-84	1335	ant	5	2.65	0.985	0	2.53E+05	4.23E+03	NIST_27900	0.00E+00	0.00E+00	KNSTD	13 593	1207	15 865	437	ED-SUERC
FLO-01-CJF	-78	-84	1357	ant	5	2.65	0.985	0	5.83E+06	5.24E+04	NIST_27900	0.00E+00	0.00E+00	KNSTD	332 953	31 633	394 185	10 254	ED-SUERC
FLO-01	-79	-84	521	ant	8	2.7	0.996	0	4.79E+04	1.99E+03	07KNSTD	0.00E+00	0.00E+00	KNSTD	5288	510	6012	283	CAMS-LLNL
FLO-02	-79	-84	521	ant	5.5	2.7	0.996	0	4.99E+04	1.48E+03	07KNSTD	0.00E+00	0.00E+00	KNSTD	5395	496	6260	231	CAMS-LLNL
FLO-03	-79	-84	521	ant	4.5	2.7	0.996	0	5.05E+04	1.12E+03	07KNSTD	0.00E+00	0.00E+00	KNSTD	5415	486	6334	197	CAMS-LLNL
FLO-05	-79	-84	521	ant	6.5	2.7	0.996	0	5.00E+04	1.32E+03	07KNSTD	0.00E+00	0.00E+00	KNSTD	5448	495	6270	215	CAMS-LLNL
FLO-06	-79	-84	515	ant	3	2.7	0.996	0	4.75E+04	1.32E+03	07KNSTD	0.00E+00	0.00E+00	KNSTD	5061	462	5994	212	CAMS-LLNL
FLO-09	-79	-84	490	ant	3	2.7	0.996	0	5.88E+04	1.78E+03	07KNSTD	0.00E+00	0.00E+00	KNSTD	6415	591	7596	283	CAMS-LLNL
FLO-10	-79	-84	490	ant	8	2.7	0.996	0	5.00E+04	1.68E+03	07KNSTD	0.00E+00	0.00E+00	KNSTD	5685	530	6464	259	CAMS-LLNL
Union Glacier																			
UG-15	-80	-81	962	ant	5	2.7	0.996	0	2.50E+06	6.40E+04	07KNSTD	0.00E+00	0.00E+00	KNSTD	190 113	18 058	223 025	7926	CAMS-LLNL
UG-16	-80	-81	938	ant	5	2.7	0.996	0	5.31E+05	1.00E+04	07KNSTD	0.00E+00	0.00E+00	KNSTD	39 660	3560	46 296	1348	CAMS-LLNL
UG-19	-80	-81	911	ant	5	2.7	0.996	0	8.80E+05	1.65E+04	07KNSTD	0.00E+00	0.00E+00	KNSTD	67 748	6123	79 187	2320	CAMS-LLNL
UG-24	-80	-81	857	ant	5	2.7	0.996	0	4.51E+05	8.42E+03	07KNSTD	0.00E+00	0.00E+00	KNSTD	36 072	3234	42 153	1221	CAMS-LLNL
UG-27	-80	-81	839	ant	5	2.7	0.996	0	4.16E+05	7.81E+03	07KNSTD	0.00E+00	0.00E+00	KNSTD	33 803	3029	39 475	1146	CAMS-LLNL
UG-30	-80	-81	800	ant	5	2.7	0.996	0	1.97E+05	6.23E+03	07KNSTD	0.00E+00	0.00E+00	KNSTD	16 544	1535	19 252	743	CAMS-LLNL

[a]Ratio of the production rate at the shielded site to that for a 2π surface at the same location calculated using the CRONUS-Earth geometric shielding calculator version 1.1.

[b]Calculated using 07KNSTD ^{10}Be measurement standard and calibration with a reported $^{10}Be/^{9}Be$ ratio $2.85 \times 10^{-12\,40}$ or to the NIST standard with an assumed isotope ratio of 2.79×10^{-11} and ^{10}Be half-life 1.36 Ma (Chmeleff *et al.* 2010, Korschinek *et al.* 2010).

[c]Model exposure age assuming no inheritance, zero erosion, density 2.65–2.7 g cm^{-3} and standard atmosphere calculated using the CRONUS-Earth ^{10}Be-^{26}Al exposure age calculator (Balco *et al.* 2008) version 2.2 using a constant production rate model and scaling scheme for spallation of Lal (1991)/Stone (2000). Ages based upon global production rate (P_{global}) and New Zealand production rate (P_{NZ}) accordingly.

[d]Ed = University of Edinburgh, SUERC = Scottish Universities Environmental Research Centre, CAMS-LLNL = Centre for Accelerator Mass Spectrometry-Lawrence Livermore National Laboratory.

Hillenbrand *et al.* 2014). Whilst the existing marine chronology is open to interpretation, including possible reworking and the potentially significant changes in Antarctic marine radiocarbon reservoir effect over time (Hillenbrand *et al.* 2014), the ages are internally coherent, suggesting that they provide reliable constraints on the gradual retreat of the grounding line across the Weddell Sea. An important constraint from the outer continental shelf records grounding line retreat, and suggests open water conditions were established by *c.* 18.1 ka (Hillenbrand *et al.* 2014). Two further reliable critical constraints exist close to the sills of the extensive Thiel and Rutford cross-shelf troughs in the Weddell Sea. These record retreat in the eastern Weddell Sea at the head of the Thiel Trough before *c.* 8.3 ka, and at the head of the Rutford Trough in the western Weddell Sea at *c.* 5.3 ka (Fig. 1) (Hillenbrand *et al.* 2014).

Terrestrial geochronological constraints

Although the available marine radiocarbon data is sparse, a more comprehensive terrestrial record of ice stream surface changes is recorded on exposed mountains in the catchments of the Rutford and Institute ice streams. This study combines new ^{10}Be and *in situ* ^{14}C data that record changes of the Rutford Ice Stream with published *in situ* ^{10}Be and ^{26}Al cosmogenic isotope data from the catchment of the Institute Ice Stream (Bentley *et al.* 2010, Fogwill *et al.* 2012). Terrestrial ice surface elevations through time are constructed by measuring cosmogenic nuclides in erratics glacially transported from sites located in the catchments of the Rutford Ice Stream and Institute Ice Stream, as suggested by our LGM ice sheet flow model (Fig. 2). Glacial erratics sampled from steep exposed bedrock surfaces, in the Flower Hills, Union Glacier, and the Patriot and Marble hills (Bentley *et al.* 2010, Fogwill *et al.* 2012) (Fig. 1), serve as 'dipsticks' that allow us to reconstruct past surface elevation changes in the catchments of the ice streams since the LGM.

Samples were reduced to pure quartz at the University of Edinburgh cosmogenic nuclide laboratory and Lawrence Livermore National Laboratories Center for Accelerator Mass Spectrometry (LLNL-CAMS) following standard procedures (Kohl & Nishiizumi 1992, Ivy-Ochs 1996, Stone 2004). The ^{10}Be ratios were measured by the AMS facility at LLNL and the Scottish Universities Environmental Research Centre (SUERC) (Xu *et al.* 2010). Measurements were standardized to the NIST SRM-4325 Be standard material with a revised nominal ^{10}Be/^{9}Be ratio of 2.79×10^{-11} (Nishiizumi *et al.* 2007). Samples were corrected for the number of ^{10}Be atoms in their associated blanks. Blanks were spiked with 250 μg ^{9}Be carrier (Edinburgh) and 474 μg ^{9}Be (LLNL-CAMS). The corresponding combined process and carrier blanks ^{10}Be/^{9}Be ratios range between $1.6–5.47 \times 10^{-15}$. Sample and blank ^{10}Be/^{9}Be analytical

uncertainties and a 2.5% carrier addition uncertainty are propagated into the 1σ analytical uncertainty for nuclide concentrations.

A version of the CRONUS-Earth online age calculator was used to determine the ^{10}Be exposure ages (Balco *et al.* 2008), implementing the New Zealand ^{10}Be production rate calibration dataset (Putnam *et al.* 2010), that uses the recently revised ^{10}Be half-life (1.387 Ma) (Chmeleff *et al.* 2010, Korschinek *et al.* 2010), and Be isotope ratio standardization of Nishiizumi (Nishiizumi *et al.* 2007). The use of this revised production rate and half-life change impact the apparent exposure ages, causing them to increase by *c.* 12% from those previously published (Bentley *et al.* 2010, Fogwill *et al.* 2012) (Table I). Choice of production rate model and scaling is often a pragmatic one and is an ongoing subject of debate. Here the New Zealand calibration dataset was used to allow comparison with other recent Antarctic studies and in the absence of an Antarctic production rate calibration site. Exposure ages are reported based on the Lal/Stone scaling model for Antarctica; using the same calibration dataset, ages differ by 2–4% depending on the choice of scaling model (Balco *et al.* 2008). The calculator uses sample thickness and density to standardize nuclide concentrations to the rock surface. The whole rock density is assumed to be 2.65–2.7 g cm^{-3}. No correction for periodic snow cover or for rock-surface erosion was included, as both of which are assumed to be negligible in these sites. An erosion rate of 0.0002 cm yr^{-1} increases ages by *c.* 2%.

Uniquely, this study also takes advantage of recent technological developments in the extraction and measurement of *in situ* radiocarbon (^{14}C) from quartz (Hippe *et al.* 2009, 2013), a cosmogenic nuclide with a considerably shorter half-life than that of ^{10}Be (^{10}Be = 1.36 x 10^{3} kyr, ^{14}C = 5.73 kyr). As the relatively short half-life of ^{14}C means that *in situ* ^{14}C acquired on exposure during interglacials decays if the sample is covered by ice during a subsequent glacial, the apparent ^{14}C age reflects the true minimum exposure age of the sample. Crucially, the disparity between the ^{10}Be and ^{14}C data allows the potential influence of prior exposure or recycling in this setting to be assessed (Lifton *et al.* 2001, White *et al.* 2011).

In situ ^{14}C extraction was performed at ETH Zürich following a modified protocol (Hippe *et al.* 2009, 2013). Quartz aliquots of *c.* 5 g were preheated at *c.* 700°C to remove atmospheric ^{14}C contamination followed by the extraction of *in situ* ^{14}C during heating to 1550–1600°C for 2 × 2 hours. The collected CO$_2$ gas was split into two samples before AMS measurement due to large gas amounts. Samples were then measured with the MICADAS AMS system using the gas ion source (Ruff *et al.* 2007, Synal *et al.* 2007, Wacker *et al.* 2010). The number of ^{14}C atoms obtained for both splits

Table II. ^{14}C cosmogenic isotope data from the Flower Hills and Union Glacier.

Sample name	AMS ID	Sample mass (g qtz)	CO$_2$ yield (μg)	Fraction modern F^{14}C[a]	±F^{14}C	δ^{13}C (‰)	(^{14}C/^{12}C)$_{Abs}$ (10^{-12})[b]	±(^{14}C/^{12}C)$_{Abs}$ (10^{-12})	^{14}C (at g^{-1})[c]	±^{14}C (at g^{-1})	Muon production rate (at g^{-1} yr^{-1})	Production rate (spallation at g^{-1} yr^{-1})[d]	^{14}C Exposure age (years)[e]	±External uncertainty (years)
FLO-18-CJFa	47425.1.1		19.8	0.835	0.010	-22.45	0.990	0.012						
FLO-18-CJFb	47425.1.2		19.6	0.854	0.010	-18.63	1.021	0.011						
Total		5.28							3.66E+05	3.92E+03	7.25	49.93	14 561	744
FLO-19-CJFa	47424.1.1		17.7	0.958	0.011	-25.37	1.129	0.013						
FLO-19-CJFb	47424.1.2		17.9	0.972	0.012	-18.62	1.162	0.014						
Total		4.98							4.00E+05	4.34E+03	7.28	50.30	18 774	961
UG16-2	47426.1.1		9.5	0.553	0.012	-28.84	0.647	0.014						
Total		0.99							2.76E+05	1.41E+04	6.20	42.48	15 101	1077
UG27a	47422.1.1		23.9	0.351	0.005	-21.61	0.416	0.006						
UG27b	47422.1.2		23.9	0.360	0.006	-20.08	0.429	0.007						
Total		5.11583							1.90E+05	3.26E+03	5.95	39.19	8081	427

[a]Normalized to δ^{13}C of -25‰$_{VPDB}$ and AD 1950.
[b]Calculated after eq. (1) in Hippe *et al.* 2009.
[c]Blank corrected; calculated after eq. (2) in Hippe *et al.* 2009.
[d]Corrected for sample thickness and topographical shielding; see Table I for correction factors.
[e]Exposure age assuming no inheritance, zero erosion, density 2.7 g cm^{-3}, with a constant production rate and scaling scheme for spallation of Lal (1991)/Stone (2000).

were summed prior to subtraction of the long-term average processing blank of $(3.15 \pm 1.19) \times 10^4$ ^{14}C atoms ($\pm$ 1 standard deviation, $n = 24$).

$^{14}Cl^{10}Be$ multi-isotope analysis

For this study, *in situ* ^{14}C exposure ages were calculated with a sea level, high latitude (SLHL) spallogenic production rate of 11.40 ± 0.9 at g^{-1} y^{-1} (Schimmelpfennig *et al.* 2014). As with ^{10}Be, the production rate was scaled to altitude and latitude according to the scaling scheme of Lal/Stone. The contribution due to muon production was calculated using the freely accessible MATLAB code of the CRONUS-Earth online calculator (http.//hess.ess.washington.edu/math/al _be_v2/P_mu_total) (Balco *et al.* 2008). In order to allow muon scaling for *in situ* ^{14}C, parameters were adjusted based on the cross sections for ^{14}C (Heisinger *et al.* 2002a, 2002b), and corrections for sample thickness and topographical shielding were applied on spallogenic production only.

Combined ^{14}C and ^{10}Be analysis is applied to sites in the Flower Hills and Union Glacier (in the catchment of the Rutford Ice Stream) which display a high percentage of anomalously 'old' apparent ^{10}Be exposure ages (Table I). The disparity between the *in situ* ^{14}C and ^{10}Be data demonstrates that the samples have experienced a complicated exposure history, suggesting either that the cosmogenic nuclide inventories of the erratics were not fully reset by glacial erosion prior to deposition, or that following initial deposition they underwent periods of exposure at different altitudes and/or cover by cold-based ice (White *et al.* 2011). Using the measured concentrations of both ^{10}Be and ^{14}C, an iterative model was constructed to calculate the maximum and minimum periods of ice cover each sample could have undergone to explain the differing nuclide concentrations. These periods were then compared with the equivalent periods of ice cover implied by the eustatic sea level data, following a similar approach to studies of the Fennoscandian Ice Sheet (Fabel *et al.* 2002).

Whilst only a one-way test, this assumes that the erratics experienced periods of ice cover subsequent to initial deposition at any point when sea level was lower (and ice volume greater) than it was at the point of re-exposure given by the ^{14}C apparent exposure age (Table II). Using the measured, minimum and maximum ^{14}C exposure ages of each sample (given by the external errors within the process, to allow for comparability with the independently dated sea level curve), three scenarios for each sample were created, under which all samples apart from UG-27 are shown to have experienced one period of extended ice cover following initial deposition, followed by subsequent re-exposure (Fig. 3). Sample UG-27 has a complex nuclide inventory, possibly reconcilable by either a single or multiple pre-exposure event at a higher altitude than
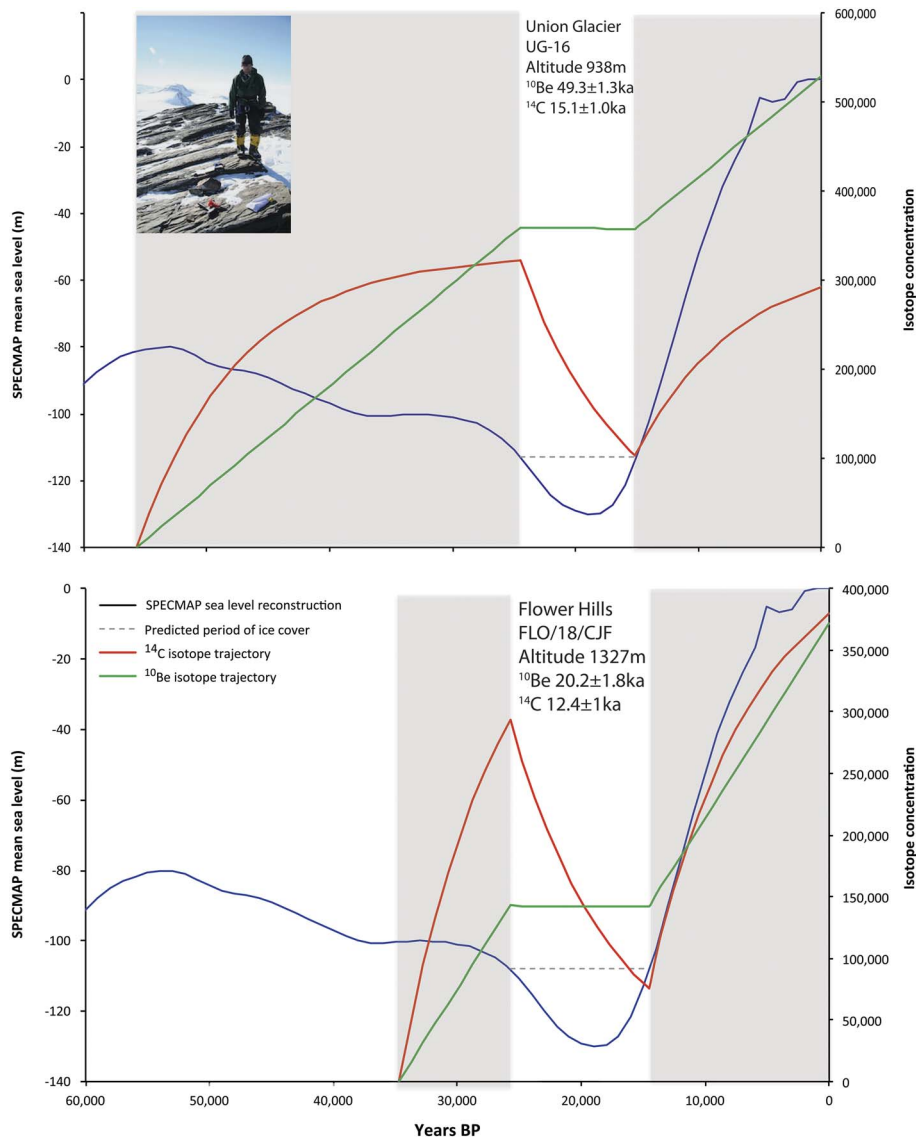
Fig. 3. Modelled relationship between $^{10}Be/^{14}C$ isotope concentrations, time and sea level used as a proxy for global ice volume (Imbrie & McIntyre 2006) for samples FLO/18/CJF and UG16. Proposed periods of sample exposure are defined by the grey boxes. The altitude and apparent exposure ages based upon the measured ^{10}Be and ^{14}C inventories of the samples are noted. The inset photo shows sample FLO/18/CJF, a quartzite erratic on striated agrilite bedrock typical of the samples analysed.

present. For the remaining samples, a scenario is identified that agrees with the periods of ice cover stipulated by the cosmogenic nuclide data and the sea level reconstruction: a single extended period of ice cover following initial deposition, and subsequent re-exposure during the last deglaciation (Fig. 3). This suggests that the disparity between the $^{14}C/^{10}Be$ is probably a result of cover by cold-based ice, and demonstrates that the use of another isotope paired alongside ^{14}C can provide insights into the depositional history of the samples, allowing for a more confident interpretation of the surface trajectory of the Rutford Ice Stream.

Results

To examine the dynamic glaciological changes recorded from our geological reconstruction, firstly the changes to geometry and ice flow pattern triggered by post-LGM

increases in oceanic heat flux and sea level were assessed. The patterns of ice flow predicted by the model under this scenario are shown in Fig. 2. The initial response of the LGM ice sheet to ocean and atmospheric forcing is depicted in Fig. 2a, and is marked by almost uniform grounding line retreat across the WSE, coupled with high discharge rates through all of the major cross-shelf troughs. The predicted ice sheet surface remains above 1300 m in the catchments of both ice streams.

Figure 2b shows the rapid increase in predicted ice flux in response to the prescribed ocean forcing, with acceleration of flow at the marine margins and concomitant drawdown of the ice sheet surface in the WSE. Although ice flux is greatest at the head of the deep Thiel Trough and its tributaries, ice from both the Rutford Ice Stream and Institute Ice Stream continue to discharge through the Rutford Trough and the extended Evans Trough on the western side of the WSE. Due to the location of the two ice
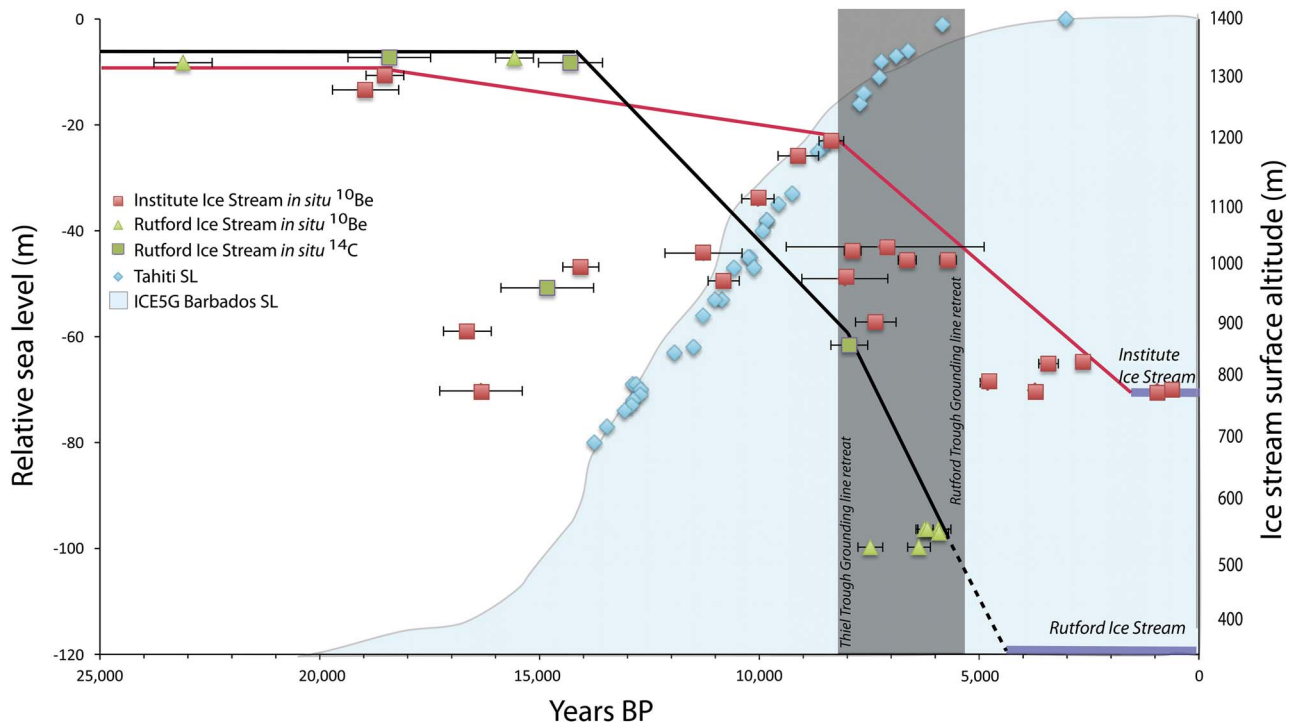
Fig. 4. Reconstructed ice stream trajectories over the last 25 000 years from terrestrial cosmogenic nuclides in glacially transported erratics (*in situ* [14]C and [10]Be ± 1 standard deviation). The profiles of the Rutford and Institute ice streams are shown in green and red, respectively. The grey column defines the timing of inner continental shelf deglaciation of the Thiel Trough and the Rutford Trough, based upon the available calibrated marine ^{14}C constraints (Hillenbrand *et al.* 2012, 2014), reflecting the proposed period of ice stream capture of the Institute Ice Stream by the Thiel Trough. For comparison, global relative sea level rise reconstructed from Tahiti (Bard *et al.* 1996, Bard 2003) and Barbados (Peltier & Fairbanks 2006) are plotted.

streams relative to the grounding line, this leads to the start of a marked and rapid drawdown of the Rutford Ice Stream at this time when compared to the Institute, reflected in rapid altitudinal change in the catchment of the Rutford Ice Stream after 15 ka (Fig. 2b).

Under continued oceanic forcing, grounding line retreat in the WSE becomes markedly asymmetric, with faster retreat taking place in the Thiel Trough (eastern WSE) than in the west (Fig. 2c upper panel). Consequently, the inland ice sheet surface gradient switches from its formerly north-easterly direction to a more east-south-easterly direction, with the effect that ice discharging in the Institute and Möller ice streams is diverted towards the Thiel Trough (Fig. 2c lower panel). Thus at this point, drainage of these neighbouring ice streams becomes governed by the locations of two separate grounding lines *c.* 300 km apart. Their behaviour is thus decoupled from one another, allowing independent thinning trajectories during deglaciation.

Discussion

The geological reconstructions presented here mirror the results of the ice sheet model simulation, and provide a

chronological framework to examine the physical effects of grounding line retreat away from the marine margin. The results demonstrate that the surface of the Rutford Ice Stream and Institute Ice Stream exceeded 1300 m in altitude at the LGM, buttressed by grounded ice in the Weddell Sea (Fig. 4, see Tables I & II for details). Geologically this upper limit of the ice stream surfaces is defined based on the absence of any apparently 'young' (post-LGM) exposure ages above this altitude (Bentley *et al.* 2010, 2011, Clark 2011), and the presence of locally derived LGM-age ice in the Patriot Hills, as demonstrated by recent analysis of the exposed blue ice in the Institute Ice Stream catchment (Turney *et al.* 2013). Based upon this interpretation it is apparent that the Rutford and Institute ice streams maintained their LGM surface profiles until 16 ka, away from the marine margins of the retreating grounding line despite rising sea level and regional ocean circulation and temperature changes (Fig. 4). This is supported by comparison of the ice stream trajectories with post-LGM eustatic global sea level, which suggest a delayed response of both the Rutford and the Institute ice streams to global sea level rise.

After *c.* 16 ka the results suggest that the surface trajectories of the two ice streams began to diverge (Fig. 4).

Initially the Institute Ice Stream thinned slowly, dropping in elevation by only 100 m between *c.* 20 and *c.* 8.5 ka. Subsequently the rate of decay increased markedly after *c.* 8.5 ka, thinning 380 m in *c.* 6000 years, to reach the present ice sheet surface elevation by *c.* 2 ka, supporting interpretations of the regional isostatic response derived from GPS constraints (Argus *et al.* 2011).

The Institute Ice Stream's surface trajectory contrasts with that of the Rutford Ice Stream, which maintained an altitude of over 1300 m until decay was initiated at *c.* 14.5 ka (Fig. 4). At this time, the Rutford apparently decayed rapidly, thinning by *c.* 900 m between *c.* 14.5 ka and *c.* 6 ka. Although the trajectory of the Rutford Ice Stream after *c.* 6 ka between the lower sample sites (520–490 m) and the present ice stream surface altitude cannot be fully defined, a lack of geomorphological evidence on the steep slopes between these altitudes suggests that the downward thinning trajectory of the Rutford Ice Stream continued in response to grounding line retreat across the inner shelf of the western Weddell Sea at *c.* 5.3 ka (Fig. 1) (Hillenbrand *et al.* 2012).

Whilst the terrestrial geological reconstruction presented here is unable to rule out if this thinning of either the Rutford or Institute ice streams continued below present levels into the late Holocene this is unlikely based upon independent evidence from the region which suggests relative stability since *c.* 4 ka (Argus *et al.* 2011, Turney *et al.* 2013). The combination of stability of ice in the catchment of the Institute Ice Stream, and the regional isostatic uplift signal argues that there was no significant recent loss (and subsequent rapid re-expansion) of the deep basins upstream of the present grounding line, as has been suggested from the interpretation of regional airborne RES (Siegert *et al.* 2013).

Together, the ice sheet model simulations and geological reconstruction presented in the this study demonstrate asymmetry in ice dynamics between the Rutford Ice Stream and Institute Ice Stream during the last glacial-interglacial transition, which realigns during the mid Holocene between *c.* 8.3 and 5.3 ka. This reflects a regional-scale diversion of ice discharge in the Institute Ice Stream due to ice stream capture by the Thiel Trough palaeo ice stream after grounding line retreat between *c.* 8.3 and 5.3 ka, which impacted regional mass balance in this sector of the WAIS (Fig. 2c). Significantly, this analysis shows that both the Institute and Möller ice streams are susceptible to capture. Additionally, this interpretation corroborates a recent interpretation of marine geophysical evidence which suggests that the Foundation Ice Stream may also be affected by ice stream flow diversion (Larter *et al.* 2012). All other modelled outlets in the western WSE continue to drain through Rutford Trough, regardless of grounding line position or dynamics.

This threshold-controlled behaviour of the Institute and Möller ice streams is probably a consequence of their central position between the two major cross-shelf troughs, implying that subglacial topography underlying the ice stream does not significantly restrict flow to a particular route. This has important ramifications for future ice sheet dynamics in the WSE, suggesting that predicted twenty-first century ocean warming in the Thiel Trough (Fogwill *et al.* 2012, Hellmer *et al.* 2014) could re-instigate capture of these ice streams. Such a divergence may lead to a marked response due to the deep subglacial basins that exist upstream of the grounding lines (Ross *et al.* 2012). Whilst previous studies have highlighted switches in ice stream direction using different approaches, including marine geophysical techniques (e.g. Larter *et al.* 2012), glaciological investigations (Conway *et al.* 2002) and ice sheet modelling studies (Payne 1999), none have been independently verified by the combined ice sheet modelling and empirical geological approach as described here.

Whilst surface exposure ages in the eastern Weddell Sea suggest that the modelled ice sheet may be too thick in this region at the LGM (Golledge *et al.* 2012), the limited thickening implied by empirical terrestrial data (Fogwill *et al.* 2004, Hein *et al.* 2011), coupled with the greatly advanced grounding line position interpreted from marine geological data (Hillenbrand *et al.* 2014), can only be reconciled with a surface slope of the LGM grounded ice sheet that is similar to that of the present ice shelf. This suggests an extremely low basal shear stress (< 15 kPa), and it is acknowledged that this disagreement with the observations requires further investigation.

In summary, the asynchronous response of the Rutford Ice Stream and Institute Ice Stream to post-LGM ice sheet reconfiguration reflects the combination of streaming ice flow and spatially variable bathymetric controls on the inner continental shelf, which caused tipping points to be passed during deglaciation, leading to jumps between stable flow patterns. Importantly, both of these major arteries of the WAIS show a remarkable delay in their response to external forcing, particularly sea level, implying that other internal mechanisms are at work. When aligned to marine records, these data reveal that the onset and rate of deglaciation of the Rutford Ice Stream and Institute Ice Stream are controlled independently by grounding line retreat within the Thiel and Rutford troughs, respectively. These findings support recent inference from marine and terrestrial geophysical surveys, which suggest that during deglaciation ice-drainage pathways in the WSE may well have differed from those observed today (Larter *et al.* 2012, Stolldorf *et al.* 2012, Siegert *et al.* 2013). Importantly, these reconstructions, together with independent constraints (Argus *et al.* 2011, Turney *et al.* 2013), do not suggest that the Institute Ice Stream has undergone significant drawdown during the late Holocene or subsequent significant re-expansion (Siegert *et al.* 2013); rather, the

results suggest that late Holocene ice stream reconfiguration of the Weddell Sea was driven by spatially variable ice flux at the marine margin, which modulated the direction of individual ice streams of the WAIS during the early Holocene.

Conclusions

The data presented here have demonstrated that two major ice streams of the WSE had an asynchronous response to ocean-forced grounding line retreat. To understand the mechanism for these divergent trends, flow changes predicted by our high-resolution ice sheet simulation, which simulated grounding line retreat in the WSE, were analysed. The decoupling of the surface trajectories of the two ice streams was driven by differences in the rate of grounding line retreat across the WSE, resulting in the Institute Ice Stream switching direction by more than 60° and discharging ice into the Thiel Trough during the early Holocene, rather than the Rutford Trough as it does at present. The new terrestrial geochronological constraints (in situ ^{14}C and ^{10}Be) reveal that although these two adjacent ice streams exhibited similar surface geometries at the end of the LGM, the pattern of ice surface lowering contrasted markedly after this, with asynchronous thinning trajectories during the late to mid Holocene.

These findings highlight that spatial variability in ice flow can trigger marked changes in the pattern, flux and flow direction of extensive ice streams on millennial timescales, markedly changing regional ice sheet mass balance. A detailed understanding of these abrupt diversions is critical to improve predictions for future WAIS stability in light of the sensitivity of the Institute Ice Stream to marine ice sheet instability today, with its present grounding line below mean sea level at the head of an extensive subglacial trough. Given this evidence of potential flow switches in the WSE, and in light of projected twenty-first century regional ocean warming in the Thiel Trough, the ability to predict these abrupt and extensive diversions is a priority within the glaciological community, achievable only through the coupling of high-resolution ice sheet and ocean models.

Acknowledgements

Author contributions

CJF, CSMT and NRG conceived the project. NRG undertook the ice sheet modelling experiments and designed the model simulation with CJF. CJF and DHR analysed the ^{10}Be samples at the University of Edinburgh and Lawrence Livermore National Laboratory, respectively. KH, RW and LW developed the ^{14}C extraction line and gas measurement techniques at ETH Zürich. CJF, DHR, KH, EBR, RSJ and RW analysed the ^{10}Be/^{14}C data interpretation. All authors discussed the results and implications, and commented on the manuscript at all stages.

References

ARGUS, D.F., BLEWITT, G., PELTIER, W.R. & KREEMER, C. 2011. Rise of the Ellsworth mountains and parts of the East Antarctic coast observed with GPS. Geophysical Research Letters, 38, 10.1029/2011GL048025.

BALCO, G., STONE, J.O., LIFTON, N.A. & DUNAI, T.J. 2008. A complete and easily accessible means of calculating surface exposure ages or erosion rates from ^{10}Be and ^{26}Al measurements. Quaternary Geochronology, 3, 174–195.

BAMBER, J.L., RIVA, R.E.M., VERMEERSEN, B.L.A. & LE BROCQ, A.M. 2009. Reassessment of the potential sea-level rise from a collapse of the West Antarctic Ice Sheet. Science, 324, 901–903.

BARD, E. 2003. Tahiti deglacial relative sea level reconstruction. IGBP PAGES/World Data Center for Paleoclimatology Data Contribution Series #2003-028. Boulder, CO: NOAA/NGDC Paleoclimatology Program.

BARD, E., HAMELIN, B., ARNOLD, M., MONTAGGIONI, L., CABIOCH, G., FAURE, G. & ROUGERIE, F. 1996. Deglacial sea level record from Tahiti corals and the timing of meltwater discharge. Nature, 382, 241–244.

BENTLEY, M.J., FOGWILL, C.J., LE BROCQ, A.M., HUBBARD, A.L., SUGDEN, D.E., DUNAI, T.J. & FREEMAN, S.P.H.T. 2010. Deglacial history of the West Antarctic Ice Sheet in the Weddell Sea embayment: constraints on past ice volume change. Geology, 38, 411–414.

BENTLEY, M.J., SUGDEN, D.E., FOGWILL, C.J., LE BROCQ, A.M., HUBBARD, A.L., DUNAI, T.J. & FREEMAN, S.P.H.T. 2011. Deglacial history of the West Antarctic Ice Sheet in the Weddell Sea embayment: constraints on past ice volume change: REPLY. Geology, 39, 10.1130/G32140Y.1.

CHMELEFF, J., VON BLANCKENBURG, F., KOSSERT, K. & JAKOB, D. 2010. Determination of the ^{10}Be half-life by multicollector ICP-MS and liquid scintillation counting. Nuclear Instruments and Methods in Physics Research, B268, 192–199.

CLARK, P.U. 2011. Deglacial history of the West Antarctic Ice Sheet in the Weddell Sea embayment: constraints on past ice volume change: COMMENT. Geology, 39, 10.1130/G31533C.1.

COMISO, J. 2000. Variability and trends in Antarctic surface temperatures from in situ and satellite infrared measurements. Journal of Climate, 13, 1674–1696.

CONWAY, H., CATANIA, G., RAYMOND, C.F., GADES, A.M., SCAMBOS, T.A. & ENGELHARDT, H. 2002. Switch of flow direction in an Antarctic ice stream. Nature, 419, 465–467.

CUFFEY, K.M. 2011. Antarctic ice flow revealed. Science, 333, 1386–1387.

Fabel, D., Stroeven, A.P., Harbor, J., Kleman, J., Elmore, D. & Fink, D. 2002. Landscape preservation under Fennoscandian ice sheets determined from *in situ* produced Be-10 and Al-26. *Earth and Planetary Science Letters*, **201**, 397–406.

Fogwill, C.J., Hein, A.S., Bentley, M.J. & Sugden, D.E. 2012. Do blue-ice moraines in the Heritage Range show the West Antarctic Ice Sheet survived the last interglacial? *Palaeogeography, Palaeoclimatology, Palaeoecology*, **335**, 61–70.

Fogwill, C.J., Bentley, M.J., Sugden, D.E., Kerr, A.R. & Kubik, P.W. 2004. Cosmogenic nuclides ^{10}Be and ^{26}Al imply limited Antarctic ice sheet thickening and low erosion in the Shackleton Range for >1 m.y. *Geology*, **32**, 265–268.

Fogwill, C.J., Turney, C.S.M., Meissner, K.J., Golledge, N.R., Spence, P., Roberts, J.L., England, M.H., Jones, R.T. & Carter, L. 2014. Testing the sensitivity of the East Antarctic Ice Sheet to Southern Ocean dynamics: past changes and future implications. *Journal of Quaternary Science*, **29**, 91–98.

Golledge, N.R., Fogwill, C.J., Mackintosh, A.N. & Buckley, K.M. 2012. Dynamics of the Last Glacial Maximum Antarctic ice-sheet and its response to ocean forcing. *Proceedings of the National Academy of Sciences of the United States of America*, **109**, 16 052–16 056.

Golledge, N.R., Levy, R.H., McKay, R.M., Fogwill, C.J., White, D.A., Graham, A.G.C., Smith, J.A., Hillenbrand, C.-D., Licht, K.J., Denton, G.H., Ackert, R.P., Maas, S.M. & Hall, B.L. 2013. Glaciology and geological signature of the Last Glacial Maximum Antarctic ice sheet. *Quaternary Science Reviews*, **78**, 225–247.

Hein, A.S., Fogwill, C.J., Sugden, D.E. & Xu, S. 2011. Glacial/interglacial ice-stream stability in the Weddell Sea embayment, Antarctica. *Earth and Planetary Science Letters*, **307**, 211–221.

Heisinger, B., Lal, D., Jull, A.J.T., Kubik, P., Ivy-Ochs, S., Knie, K. & Nolte, E. 2002a. Production of selected cosmogenic radionuclides by muons. 2. Capture of negative muons. *Earth and Planetary Science Letters*, **200**, 357–369.

Heisinger, B., Lal, D., Jull, A.J.T., Kubik, P., Ivy-Ochs, S., Neumaier, S., Knie, K., Lazarev, V. & Nolte, E. 2002b. Production of selected cosmogenic radionuclides by muons. 1. Fast muons. *Earth and Planetary Science Letters*, **200**, 345–355.

Hellmer, H.H., Kauker, F., Timmermann, R., Determann, J. & Rae, J. 2012. Twenty-first-century warming of a large Antarctic ice-shelf cavity by a redirected coastal current. *Nature*, **485**, 225–228.

Hillenbrand, C.D., Melles, M., Kuhn, G. & Larter, R.D. 2012. Marine geological constraints for the grounding-line position of the Antarctic ice sheet on the southern Weddell Sea shelf at the Last Glacial Maximum. *Quaternary Science Reviews*, **32**, 25–47.

Hillenbrand, C.D., Bentley, M.J., Stolldorf, T.D., Hein, A.S., Kuhn, G., Graham, A.G.C., Fogwill, C.J., Kristoffersen, Y., Smith, J.A., Anderson, J.B., Larter, R.D., Melles, M., Hodgson, D., Mulvaney, R. & Sugden, D.E. 2014. Reconstruction of changes in the Weddell Sea sector of the Antarctic Ice Sheet since the Last Glacial Maximum. *Quaternary Science Reviews*, 10.1016/j.quascirev.2013.10.016.

Hippe, K., Kober, F., Baur, H., Ruff, M., Wacker, L. & Wieler, R. 2009. The current performance of the *in situ* ^{14}C extraction line at ETH. *Quaternary Geochronology*, **4**, 493–500.

Hippe, K., Kober, F., Wacker, L., Fahrni, S.M., Ivy-Ochs, S., Akçar, N., Schlüchter, C. & Wieler, R. 2013. An update on *in situ* cosmogenic ^{14}C analysis at ETH Zürich. *Nuclear Instruments and Methods in Physics Research Section*, **B294**, 81–86.

Imbrie, J.D. & McIntyre, A. 2006. SPECMAP time scale developed by Imbrie *et al.* 1984 based on normalized planktonic records (normalized O-18 vs time, specmap.017). *Earth System Science Data*, 10.15941PANGAEA.441706

Ivy-Ochs, S. 1996. *The dating of rock surfaces using in situ produced ^{10}Be, ^{26}Al and ^{36}Cl, with examples from Antarctica and the Swiss Alps*. PhD thesis, Zurich ETH, 197 pp. [Unpublished].

Kohl, C.P. & Nishiizumi, K. 1992. Chemical isolation of quartz for measurement of in-situ produced cosmogenic nuclides. *Geochimica et Cosmochimica Acta*, **56**, 3583–3587.

Korschinek, G., Bergmaier, A., Faestermann, T., *et al.* 2010. A new value for the half-life of ^{10}Be by heavy-ion elastic recoil detection and liquid scintillation counting. *Nuclear Instruments and Methods in Physics Research Section*, **B268**, 187–191.

Larter, R.D., Graham, A.G.C., Hillenbrand, C.-D., Smith, J.A. & Gales, J.A. 2012. Late Quaternary grounded ice extent in the Filchner Trough, Weddell Sea, Antarctica. new marine geophysical evidence. *Quaternary Science Reviews*, **53**, 111–122.

Le Brocq, A., Payne, A. & Vieli, A. 2010. An improved Antarctic dataset for high resolution numerical ice sheet models (ALBMAP v1). *Earth System Science Data*, **2**, 247–260.

Lifton, N.A., Jull, A.J.T. & Quade, J. 2001. A new extraction technique and production rate estimate for in situ cosmogenic ^{14}C in quartz. *Geochimica et Cosmochimica Acta*, **65**, 1953–1969.

Lisiecki, L.E. & Raymo, M.E. 2005. A Pliocene-Pleistocene stack of 57 globally distributed benthic ^{18}O records. *Paleoceanography*, **20**, 10.1029/2004PA001071.

Nishiizumi, K., Imamura, M., Caffee, M.W., Southon, J.R., Finkel, R.C. & McAninch, J. 2007. Absolute calibration of ^{10}Be AMS standards. *Nuclear Instruments and Methods in Physics Research Section*, **B258**, 403–413.

Payne, A.J. 1999. A thermomechanical model of ice flow in West Antarctica. *Climate Dynamics*, **15**, 115–125.

Peltier, W.R. & Fairbanks, R.G. 2006. Global glacial ice volume and Last Glacial Maximum duration from an extended Barbados sea level record. *Quaternary Science Reviews*, **25**, 3322–3337.

Petit, J.R., Jouzel, J., Raynaud, D., *et al.* 1999. Climate and atmospheric history of the past 420,000 years from the Vostok ice core, Antarctica. *Nature*, **399**, 429–436.

Putnam, A.E., Schaefer, J.M., Barrell, D.J.A., Vandergoes, M., Denton, G.H., Kaplan, M.R., Finkel, R.C., Schwartz, R., Goehring, B.M. & Kelley, S.E. 2010. *In situ* cosmogenic ^{10}Be production-rate calibration from the Southern Alps, New Zealand. *Quaternary Geochronology*, **5**, 392–409.

Rignot, E., Mouginot, J. & Scheuchl, B. 2011. Ice flow of the Antarctic ice sheet. *Science*, **333**, 1427–1430.

Rignot, E., Mouginot, J., Morlighem, M., Seroussi, H. & Scheuchl, B. 2014. Widespread, rapid grounding line retreat of Pine Island, Thwaites, Smith and Kohler glaciers, West Antarctica from 1992 to 2011. *Geophysical Research Letters*, **41**, 3502–3509.

Ross, N., Bingham, R.G., Corr, H.F.J., Ferraccioli, F., Jordan, T.A., Le Brocq, A., Rippin, D.M., Young, D., Blankenship, D.D. & Siegert, M.J. 2012. Steep reverse bed slope at the grounding line of the Weddell Sea sector in West Antarctica. *Nature Geoscience*, **5**, 393–396.

Ruff, M., Wacker, L., Gaggeler, H.W., Suter, M., Synal, H.A. & Szidat, S. 2007. A gas ion source for radiocarbon measurements at 200 kV. *Radiocarbon*, **49**, 307–314.

Schimmelpfennig, I., Schaefer, J.M., Akçar, N., Koffman, T., Ivy-Ochs, S., Schwartz, R., Finkel, R.C., Zimmerman, S. & Schlüchter, C. 2014. A chronology of Holocene and Little Ice Age glacier culminations of the Steingletscher, Central Alps, Switzerland, based on high-sensitivity beryllium-10 moraine dating. *Earth and Planetary Science Letters*, **393**, 220–230.

Shapiro, N.M. & Ritzwoller, M.H. 2004. Inferring surface heat flux distributions guided by a global seismic model: particular application to Antarctica. *Earth and Planetary Science Letters*, **223**, 213–224.

Siegert, M., Ross, N., Corr, H., Kingslake, J. & Hindmarsh, R. 2013. Late Holocene ice-flow reconfiguration in the Weddell Sea sector of West Antarctica. *Quaternary Science Reviews*, **78**, 98–107.

STOLLDORF, T., SCHENKE, H.W. & ANDERSON, J.B. 2012. LGM ice sheet extent in the Weddell Sea. evidence for diachronous behavior of Antarctic ice sheets. *Quaternary Science Reviews*, **48**, 20–31.

STONE, J.O. 2004. Extraction of Al and Be from quartz for isotopic analysis. Seattle, WA: Cosmogenic Nuclide Laboratories at the University of Washington, 8 pp. Available at: http://depts. washington.edu/cosmolab/chem/Al-26_Be-10.pdf.

SYNAL, H.A., STOCKER, M. & SUTER, M. 2007. MICADAS: a new compact radiocarbon AMS system. *Instruments and Methods in Physics Research*, **B259**, 7–13.

THOMAS, R.H. & BENTLEY, C.R. 1978. A model for Holocene retreat of the West Antarctic Ice Sheet. *Quaternary Research*, **10**, 150–170.

TURNEY, C., FOGWILL, C., VAN OMMEN, T.D., MOY, A.D., ETHERIDGE, D., RUBINO, M., CURRAN, M.A.J. & RIVERA, A. 2013. Late Pleistocene and early Holocene change in the Weddell Sea: a new climate record from the Patriot Hills, Ellsworth Mountains, West Antarctica. *Journal of Quaternary Science*, **28**, 697–704.

VAN DE BERG, W.J., VAN DEN BROEKE, M.R., REIJMER, C.H. & VAN MEIJGAARD, E. 2006. Reassessment of the Antarctic surface mass balance using calibrated output of a regional atmospheric climate model. *Journal of Geophysical Research - Atmospheres*, **111**, 10.1029/2005JD006495.

WACKER, L., BONANI, G., FRIEDRICH, M., HAJDAS, I., KROMER, B., NEMEC, M., RUFF, M., SUTER, M., SYNAL, H.A. & VOCKENHUBER, C. 2010. MICADAS: routine and high-precision radiocarbon dating. *Radiocarbon*, **52**, 252–262.

WEERTMAN, J. 1974. Stability of the junction of an ice sheet and an ice shelf. *Journal of Glaciology*, **13**, 3–11.

WHITE, D., FÜLÖP, R.H., BISHOP, P., MACKINTOSH, A. & COOK, G. 2011. Can in-situ cosmogenic ^{14}C be used to assess the influence of clast recycling on exposure dating of ice retreat in Antarctica? *Quaternary Geochronology*, **6**, 289–294.

XU, S., DOUGANS, A.B., FREEMAN, S.P.H.T., SCHNABEL, C. & WILCKEN, K.M. 2010. Improved [10]Be and [26]Al-AMS with a 5MV spectrometer. *Nuclear Instruments and Methods in Physics Research Section*, **B268**, 736–738.